Supplementary Information for

Title: The Kuroshio flowing over seamounts and associated submesoscale flows drive 100-km-wide 100-1000-fold enhancement of turbulence

Authors: Takeyoshi Nagai[1]*, Daisuke Hasegawa[2†], Eisuke Tsutusmi[3†], Hirohiko Nakamura[4†], Ayako Nishina[4†], Tomoharu Senjyu[3†], Takahiro Endoh[3†], Takeshi Matsuno[3†], Ryuichiro Inoue[5†], Amit Tandon[6†]

*Correspondence to: takeyoshi@gmail.com

This PDF file includes:

Figs. S1 to S13

References

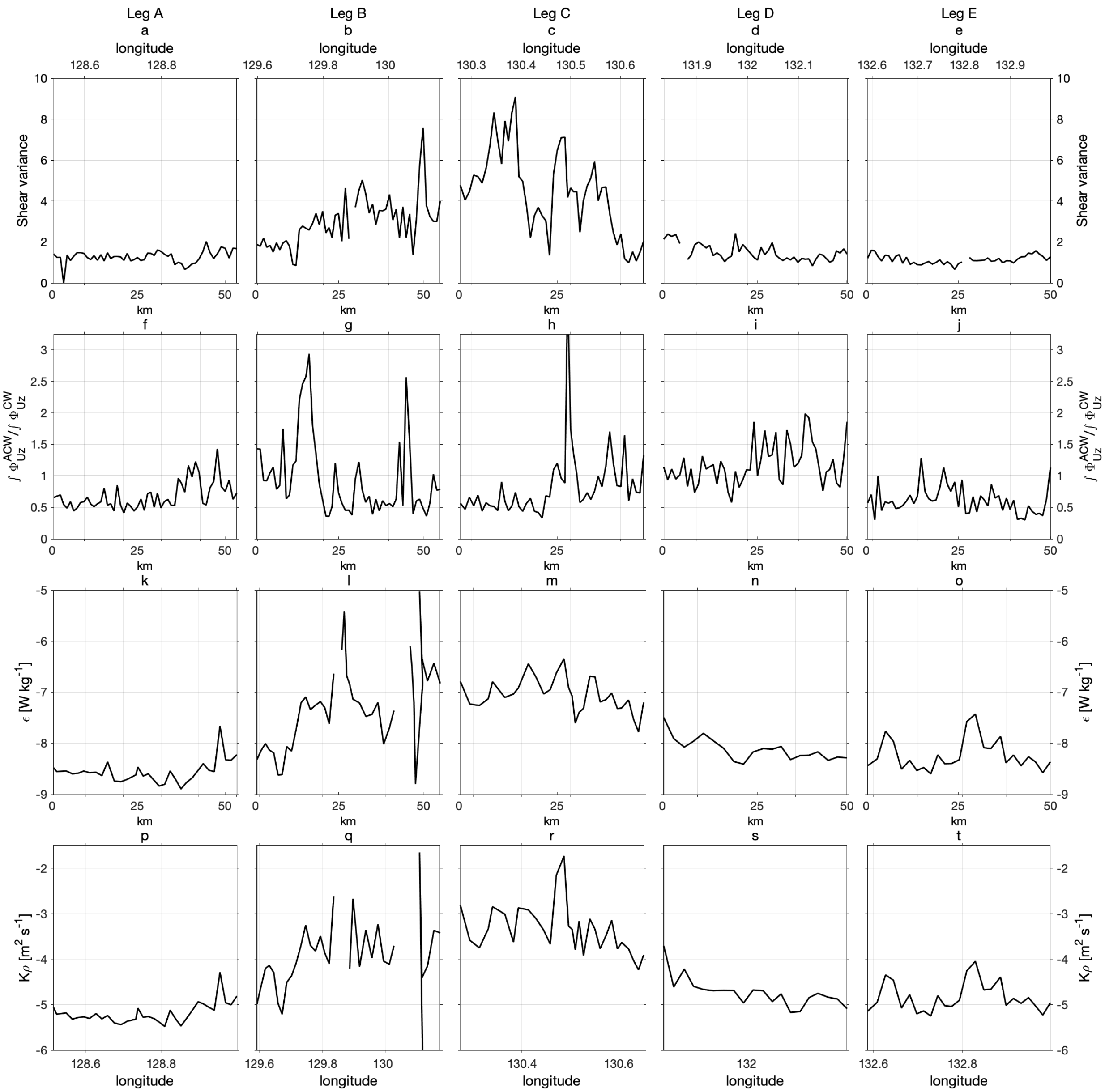

Fig. S1 | Transitions along the Kuroshio, for (a-e) depth-averaged shipboard ADCP shear variance (10^{-5} s^{-2}) along the Kuroshio, (f-j) the ratio of the anticlockwise rotating component of the integrated wavenumber rotary spectrum to that of clockwise rotating component $\int \phi_{u_z}^{ACW} / \int \phi_{u_z}^{CW}$ for each leg. Values of this ratio > 1 indicate upward energy propagation due to internal waves and < 1 represent downward energy propagation. Curves in (k-o) show the depth-averaged dissipation rates ($\log_{10}$ Wkg^{-1}), and those in (p-t) show cureves for vertical turbulent eddy diffusivity ($\log_{10}$ m^2 s^{-1}). During the November 2017 cruise, the shipboard ADCP shear along the Kuroshio axis became amplified near the seamount in the Tokara Strait. The anticlockwise shear rotation with depth dominated near the seamounts (g and h), suggesting upward energy propagation by internal waves. The shear variance was amplified by a factor of 5 near the seamounts (b and c). The depth-averaged dissipation rates below 100 m show O(10^{-7}–10^{-6} Wkg^{-1}) over 100 km path near the seamounts (l and m), which are 100- to 1000-fold enhanced compared to that away from the seamounts (k and o).

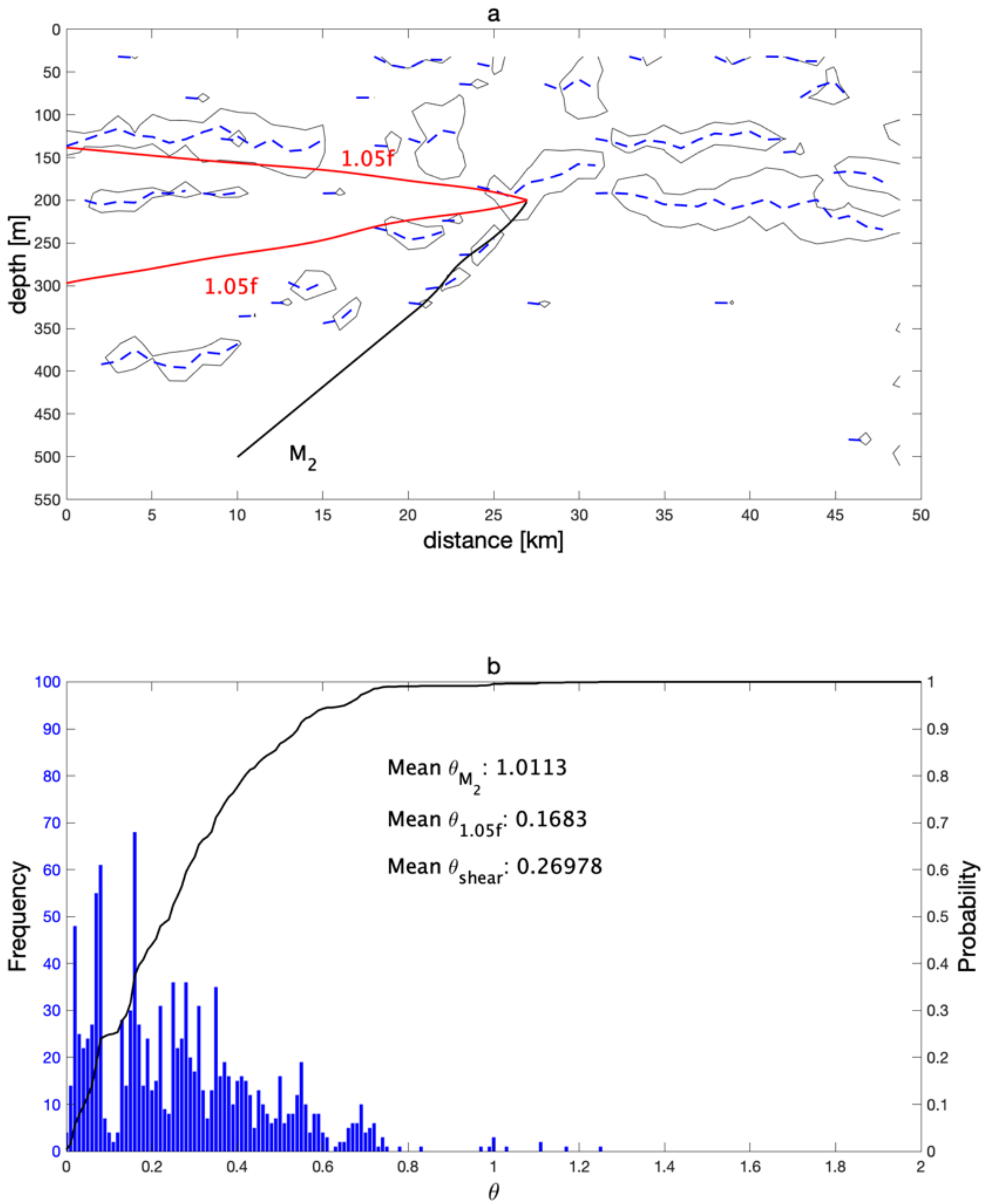

Fig. S2 | Angle of banded shear and that of internal-wave ray paths. (a) Black contour shows back rotated shear at 0.003 s^{-1}. The dashed blue lines are average depths of the contours as a function of distance. Solid lines are the internal-wave ray paths at (red) near-inertial 1.05f and (black) M_2 tidal frequency. (b) Blue bar shows the histogram of the angles θ (degree) formed from the horizon for the average shear contours (dashed blue lines in (a)). Black curve shows its cumulative probability function. Texts in panel (b) indicate mean angles of the internal-wave ray paths for each frequency, and that for the shear contours.

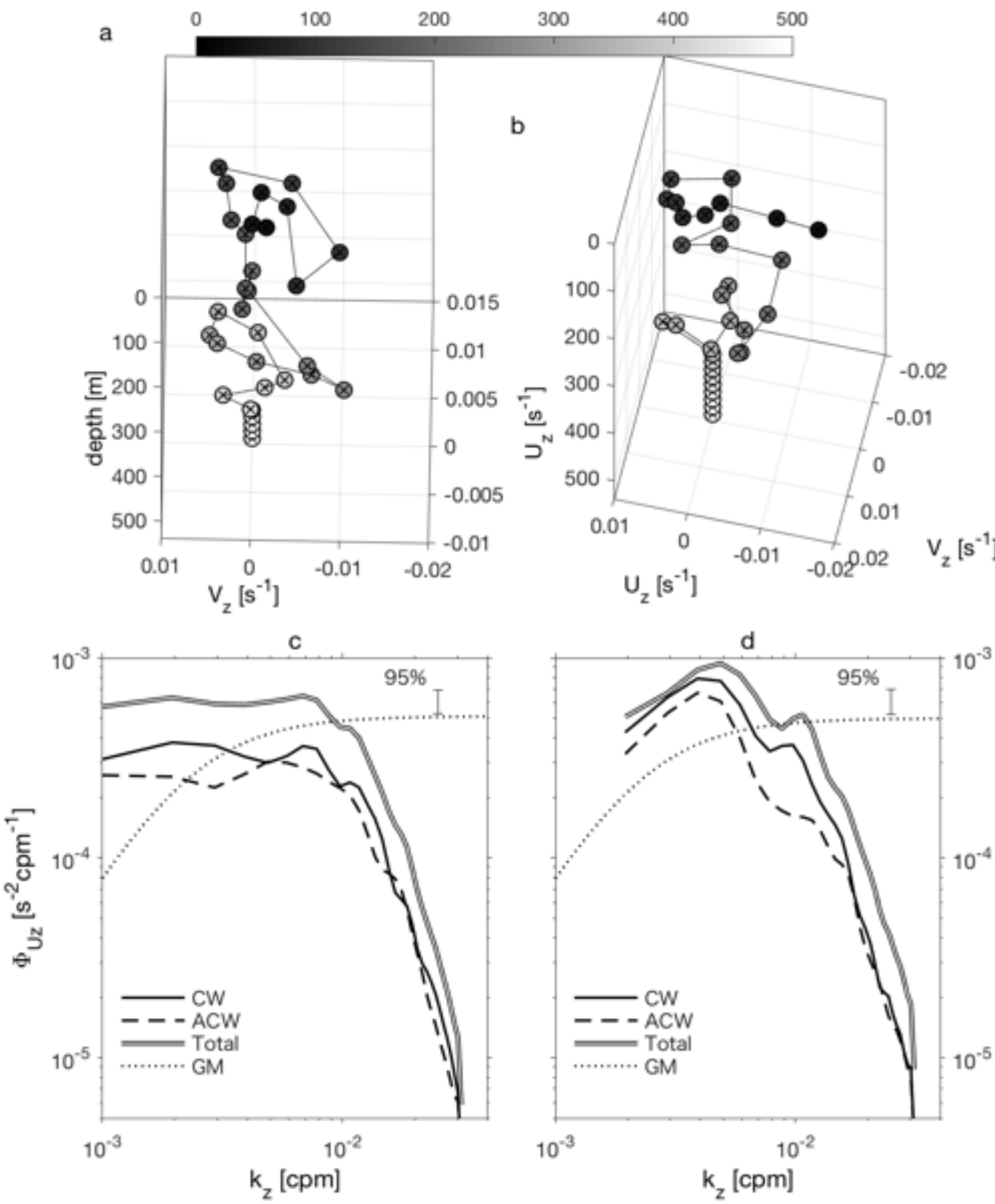

Fig. S3 | Rotation of shear vector with depth. (a) Hodographs of shear at 129.78°E in Leg b, and (b) that at 130.36°E in Leg c. Shading indicates the depth (m). Rotary spectra of shear are shown in the bottom panels by solid curves for clockwise rotation (CW) with depth and dashed curves for anticlockwise component (ACW) for (c) Leg b and (d) Leg c. Black-white-black curve = the total shear and the error bar represents 95% confidence intervals. Dotted curve = Garrett-Munk internal-wave shear spectra.

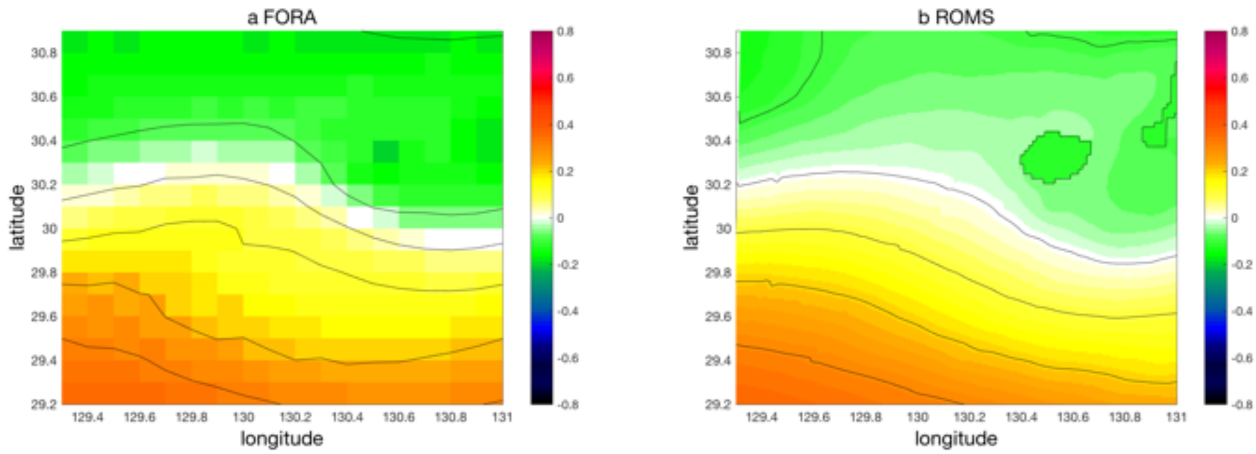

Fig. S4 | Comparison of sea surface height between ocean reanalysis and simulation in this study. Model sea surface height [m] averaged (b) during October to December is compared with (a) the FORA reanalysis averaged for the same months from 2004 through 2014. The Four-dimensional variational Ocean Reanalysis for the western North Pacific (FORA-WNP30) is a 0.1 degree horizontal resolution re-analysis dataset produced by the Japan Agency for Marine-Earth Science and Technology (JAMSTEC) and the Japan Meteorological Agency/Meteorological Institute (JMA/MRI) for 1982-2014 (*1*).

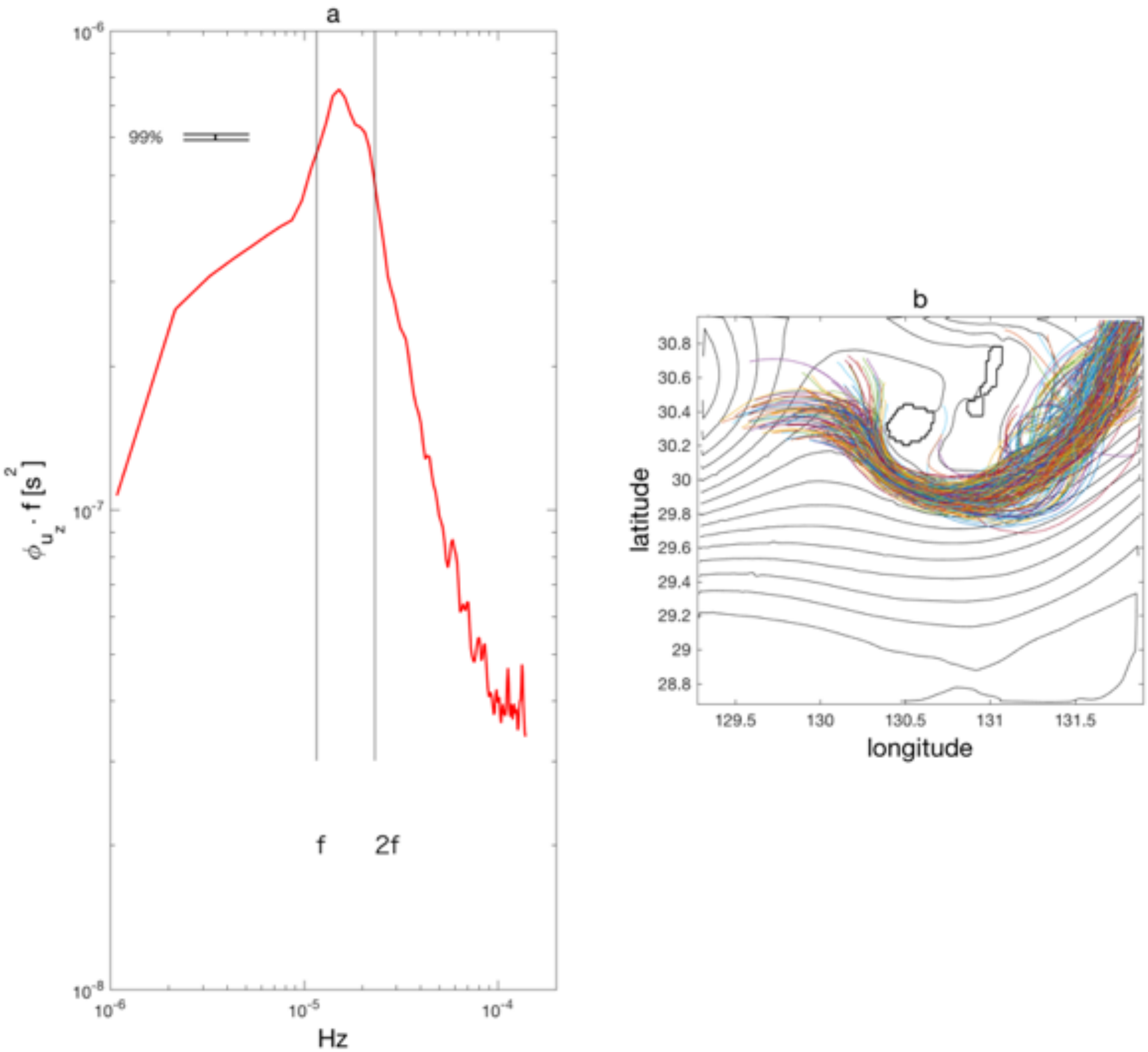

Fig. S5 | Lagrangian frequency spectrum for model shear. (a) Average Lagrangian shear spectrum for zonal velocity shear recorded along 261 Lagrangian particles which show average velocity magnitude greater than 0.85 ms^{-1}, with an error bar that represents a 99% confidence interval. The particle trajectories are shown with colored curves in (b) with contours of average model sea surface height. Model vertical shear exhibits banded high vertical wavenumber structures along the isopycnals, which are amplified near the seamounts in the modeled Kuroshio. To identify the frequency of these fluctuations avoiding Doppler-shift, 12,000 Lagrangian particles were re-released from the upstream side of the Tokara Strait, and the vertical shear was tracked along each trajectory of the Lagrangian particle.

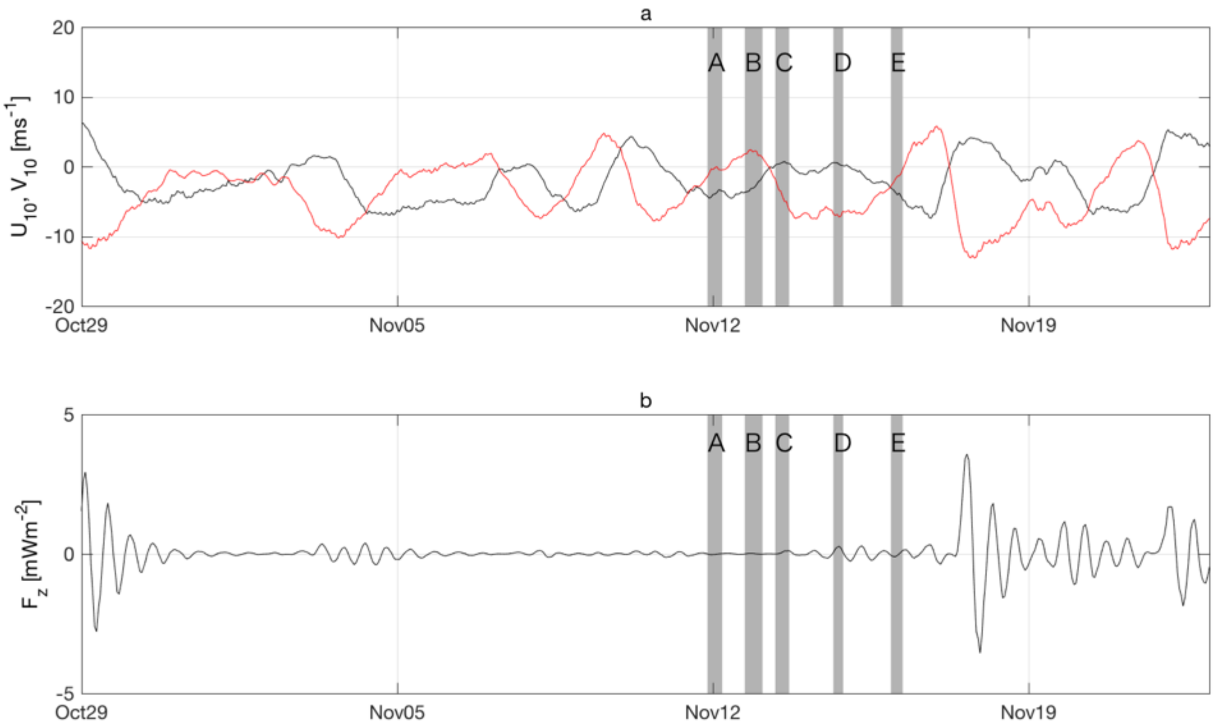

Fig. S6 | Wind effects during the observations using (a) GPV-MSM (Grid Point Values-mesoscale non-hydrostatic model, Japan Meteorological Agency, Saito *et al*. 2006) wind speed averaged over the study region between 26-33°N and 127-134°E for zonal (black) and meridional (red) components (m s^{-1}). (b) Estimated energy flux from the wind into near-inertial motions using a slab model (Pollard and Millard 1970 (*2*)) with the hourly GPV winds. Observation time spans are indicated as shadings for Leg a-e.

The wind is the main source of the near-inertial internal waves in the ocean. However, the results of this study suggest that the contribution by the Kuroshio flow over seamounts dominates the generation of the high vertical wavenumber near-inertial internal waves in the vicinity of the seamounts. To clarify whether the wind during the observations could be the source of the near-inertial internal waves, a slab mixed layer model (Pollard and Millard 1970) (*2*) was used to estimate near-inertial energy input from the wind. The wind record was obtained from GPV-MSM (Grid Point Values-mesoscale non-hydrostatic model) reanalysis winds (Japan Meteorological Agency) (*3*) averaged over the study region between 26-33°N and 127-134°E, which includes the Tokara Strait. The estimated wind energy input to the inertial oscillation shows relatively small values, within $\pm$1 mWm^{-2} during the observations in Legs a-e. After averaging the wind energy input during the period from November 12-16 for Legs a–e, +4.13 x 10^{-3} mWm^{-2} was obtained, suggesting a very small net energy gain for the inertial oscillation. This suggests that wind input cannot explain the observed intensification of the near-inertial internal waves near the seamounts during the period from November 12-16.

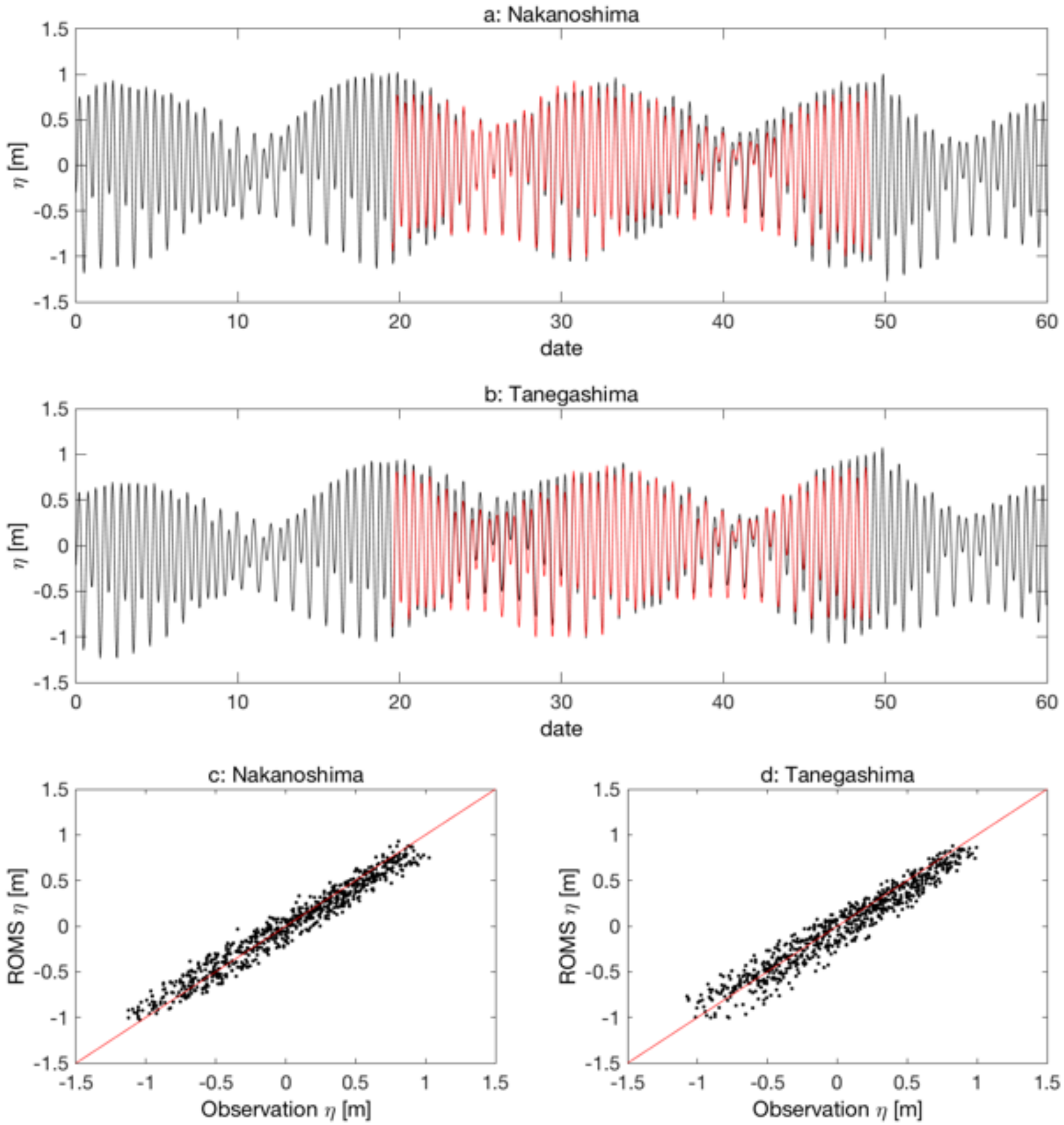

Fig. S7 | Simulation with tidal forcing. Comparison of the hourly surface elevation between observations (black) and simulation (red) at (a) Nakanoshima tidal station (29ºN 50.517’ 129ºE 50.867’) and (b) Tanegashima tidal station (30ºN 27.816’ 130ºE 57.864’). Scatter plot of the observed and simulated hourly surface elevation at (c) Nakanoshima tidal station and (d) Tanegashima tidal station.

Although the negative PV generation and associated inertial–symmetric instability is suggested by observations and numerical simulation, the effects of tidal forcing, which may generate internal tides and alter the flow time evolution, are not considered in the initial simulation. To ascertain whether the Kuroshio induced inertial–symmetric instability and generation of near-inertial internal waves are the dominant mechanism for the observed enormous scales of very strong turbulence, the same numerical simulation was repeated with realistic tidal forcing. The tidal surface elevation and velocity are forced from the open boundaries of the level 2 nested grid. Tidal constituents M_2, S_2, N_2, K_1, O_1 are included. The simulated surface elevation shows good agreement with the observations at Nakanoshima and Tanegashima tidal stations. The respective correlation coefficients for Nakanoshima and Tanegashima tidal stations are 0.98 and 0.97. The negative PV generations (Supplementary materials Fig. S8f) and associated energy dissipation rates (Supplementary materials Fig. S8e, g and h) are found also with tidal forcing.

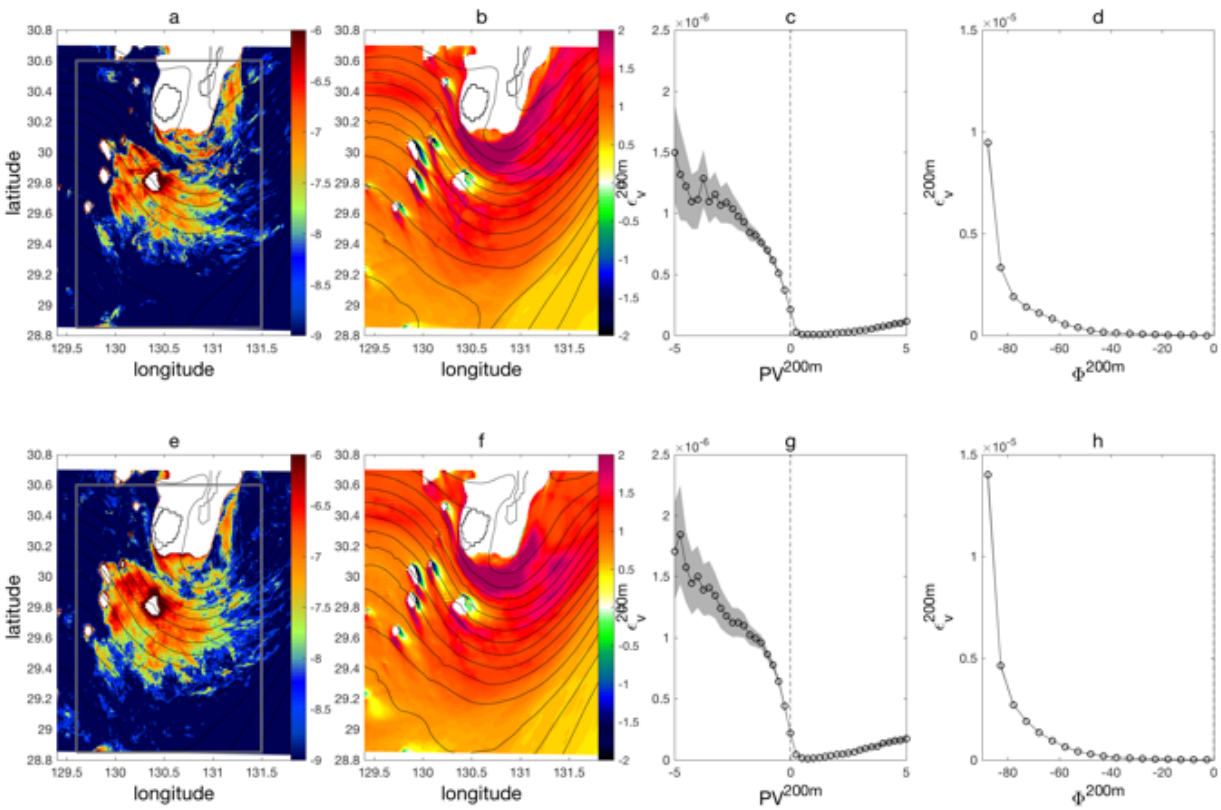

Fig. S8 | Model kinetic energy dissipation, potential vorticity (PV) and Thomas angle (Φ). Monthly averaged model kinetic energy dissipation caused by vertical shear alone for (a) without tide and for (e) with tidal forcing. Boxes in (a) and (e) represent the domains for integrating the modeled total dissipation rate by the Tokara Strait. Average modeled PV at 200 m depth is shown for (b) without tide and for (f) with tidal forcing. The hourly kinetic energy dissipation rate through the vertical shear term at 200 m depth is averaged as a function of hourly average PV at 200 m depth and shown in (c) for the case without tidal forcing and for (g) for with the tidal forcing. The hourly kinetic energy dissipation rate only with negative PV is averaged as a function of Thomas angle Φ (*7*) and shown in (d) for the case without tidal forcing and (h) for the tidal forcing case. Shading in (c-d and g-h) represents the 95% confidence interval, although confidence interval is very narrow and almost invisible in (d and h).

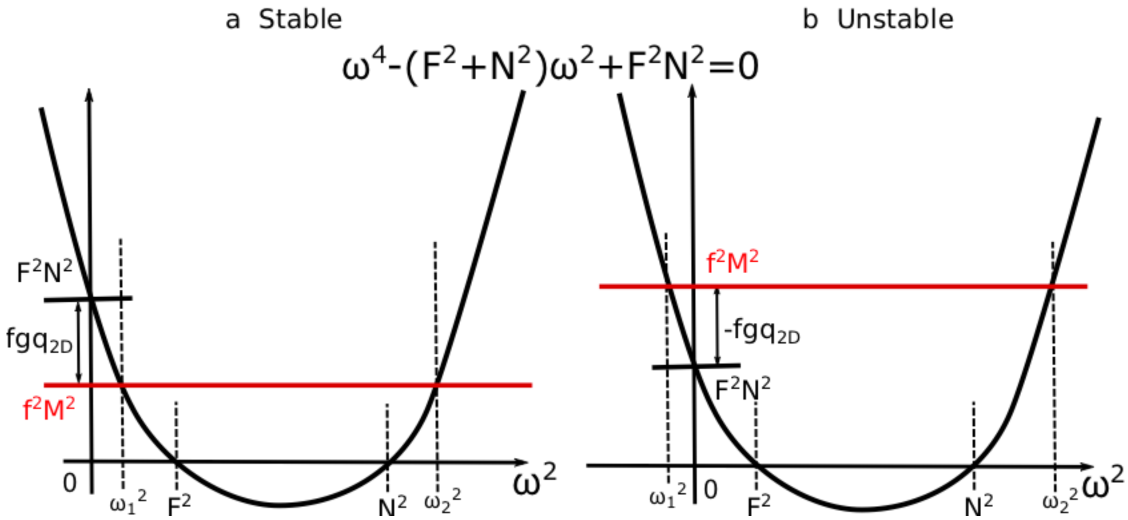

Fig. S9 | Schematics for a symmetric instability solution. The frequency ω of the solution for the perturbation flow in a two-dimensional (*x*-*z*) meridional front can be written as, $\omega^4 - (F^2 + N^2)\omega^2 + F^2N^2 = f^2M^2$, where $F^2 = f(f + v_x)$ with f the Coriolis parameter, *v* the meridional velocity, subscript *x* representing the zonal derivative, N^2 the buoyancy frequency square, and $M = v_z$ the vertical shear of meridional flow. Note that using the last term on the left hand side, the term on the right hand side, and the thermal-wind relation, $fv_x = b_x$, where *b* is buoyancy, two-dimensional potential vorticity, PV, can be re-written as

$$F^2N^2 - f^2M^2 = f(f + v_x)b_z - f^2v_z^2$$
$$= -\frac{g}{\rho_o}[f(f + v_x)\rho_z - f\rho_x v_z] = fgq_{2D}$$

The two solutions of the equation can be visualized as in Supplementary materials Fig. S9. When $fgq_{2D} < 0$, then one of the solutions for ω_1^2 becomes negative, which leads to exponential growth of the perturbation, and hence instability. When $fgq_{2D} > 0$ with $0 < F^2 < N^2$, the stable solution ω_1^2 is in the range, $0 < \omega_1^2 \leq F^2$, and ω_2^2 is found in the range, $N^2 < \omega_2^2$. The anomalously lower $0 < \omega^2 < F^2$ and higher $N^2 < \omega^2$ frequency internal waves than that without the front, $f^2 < \omega^2 < N^2$, are possible because of geostrophic horizontal and vertical shear (Mooers 1985; Kunze 1985; Whitt and Thomas 2013) (*4*-*6*).

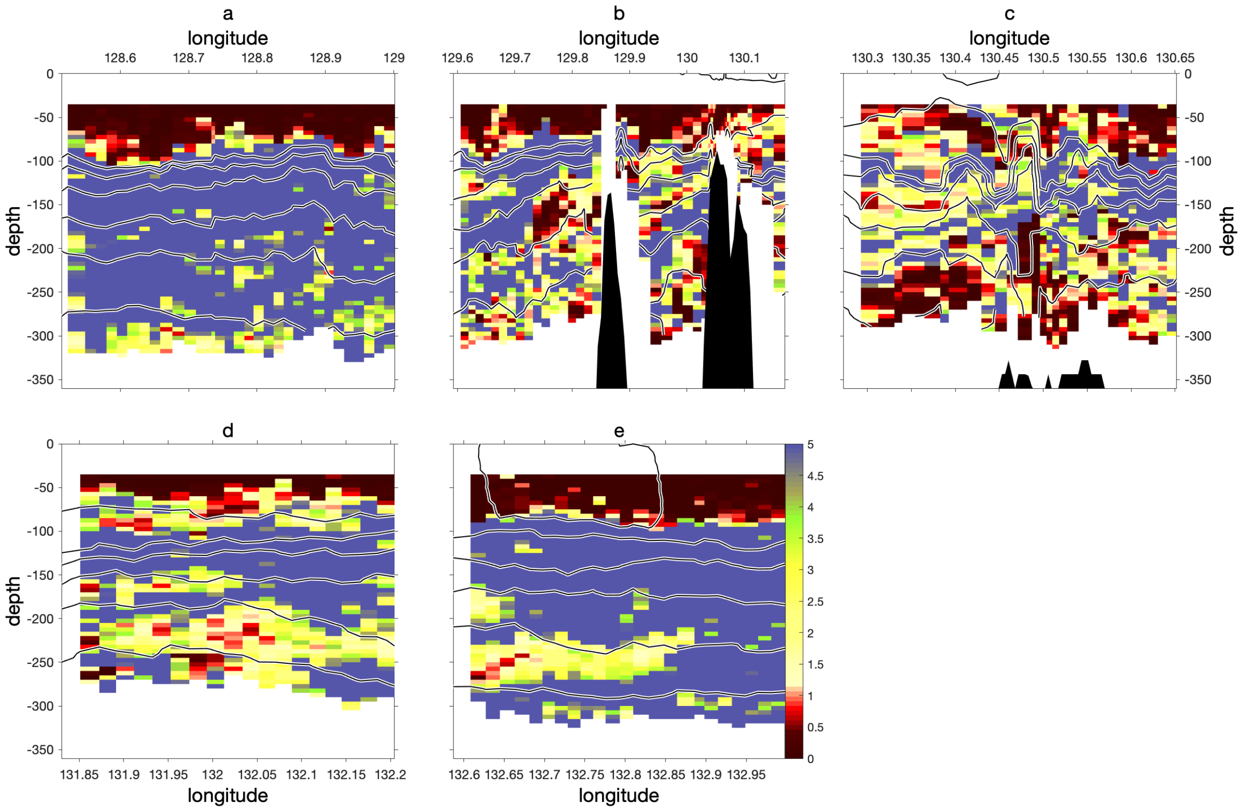

Fig. S10 | 8-m-ADCP derived Richardson number during November 2017 cruise. (a) for Leg a, (b) Leg b, (c) Leg c, (d) Leg d, and (e) Leg e cruise. Color represents the Richardson number in linear scale. Contours indicate isopycnals as in the Fig. 1. Seamount topography in the Tokara Strait is shown as black in (b-c).

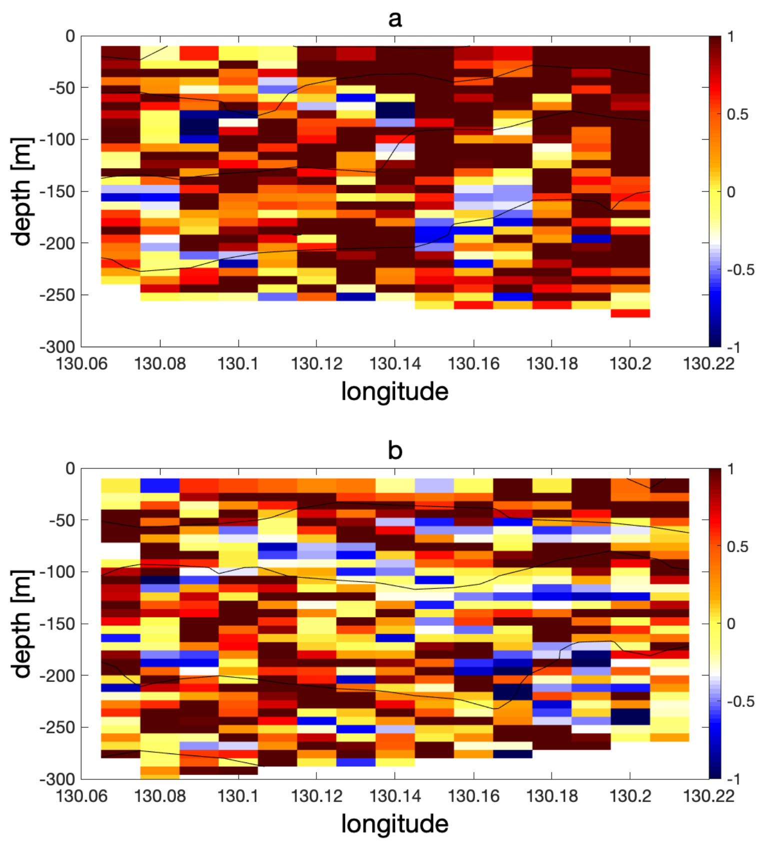

Fig. S11 | Vertical sections of 8-m-ADCP Richardson number during June 2018 cruise. (a) for the line along the red line in Fig. 4 and (b) along the blue line in Fig. 4. Color is in log scale and black contour represents isopycnal.

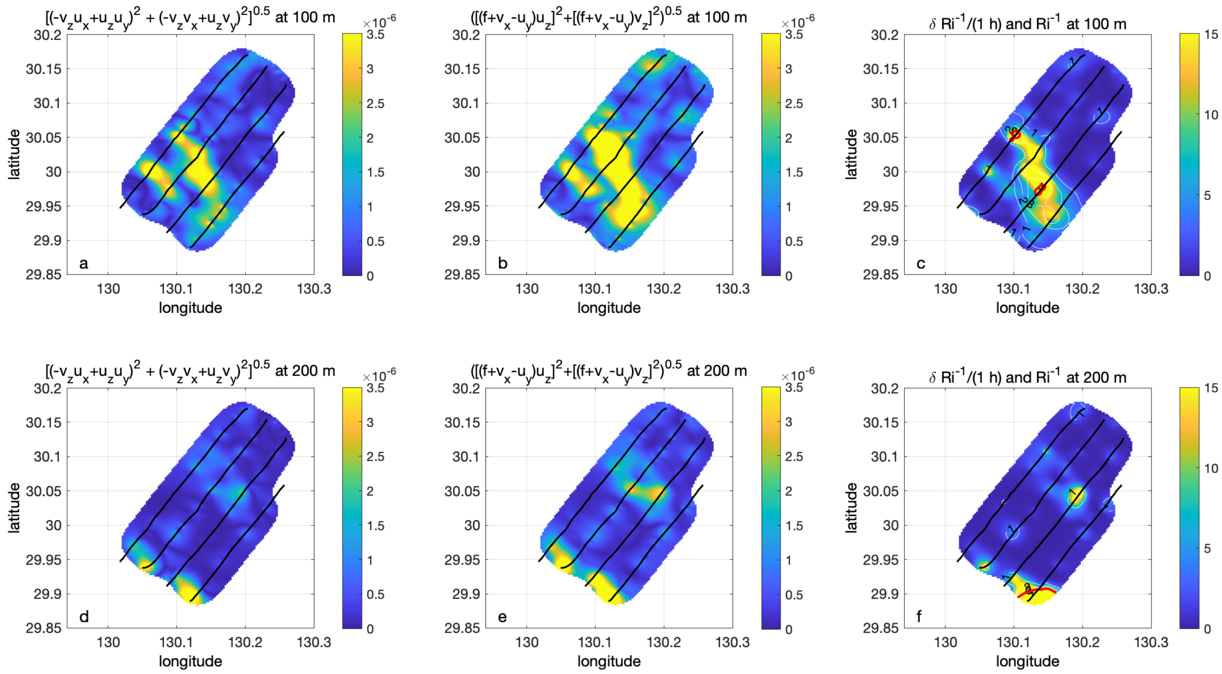

Fig. S12 | Magnitude of rate of change of vertical shear during November 2019 cruise. (a and d) show tilting and stretching of the vertical shear, (b and e) tilting of the vertical relative vorticity by vertical shear. (c and f) show change of Ri^{-1} in 1 hour by the vorticity tilt and stretch from their local value. (a-c) are at 100 m and (d-f) 200 m depth. The contours in (c and f) are Ri^{-1}, and that at $Ri^{-1} = 4$ is shown in red. These terms are computed using mapped three-dimensional flow and density, which are used to obtain PV.

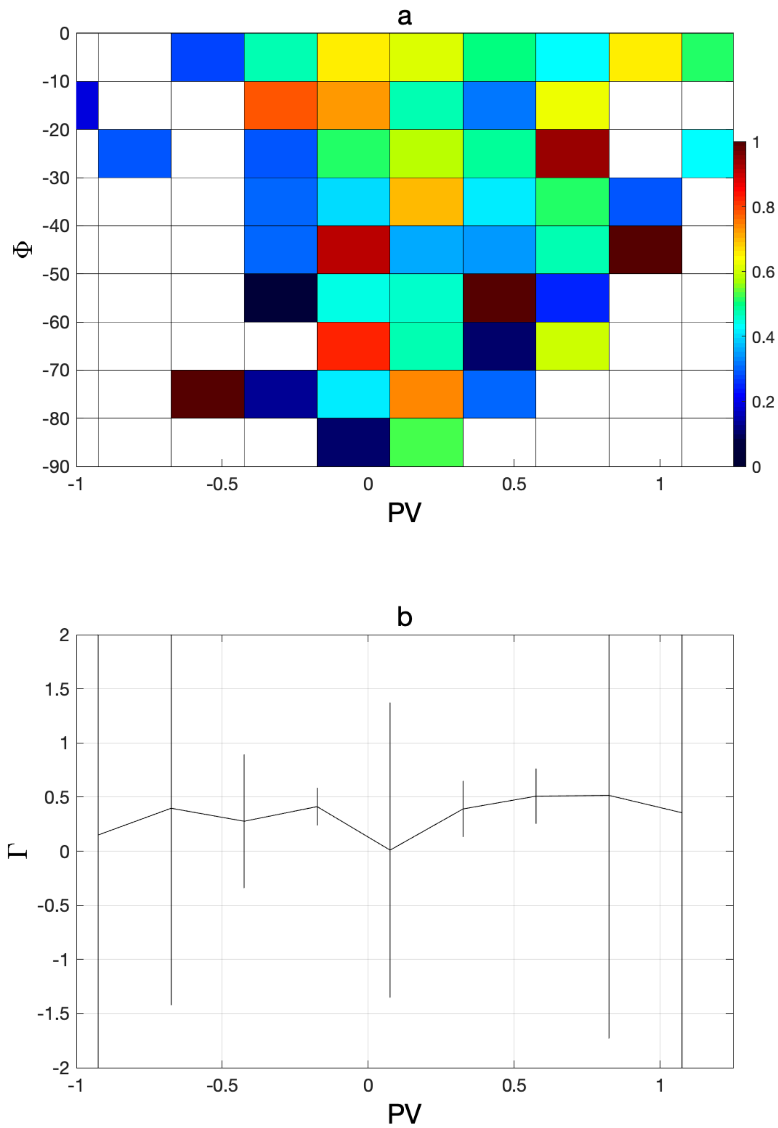

Fig. S13 | Mixing efficiency factor during June 2018 cruise. (a) Bin-average mixing efficiency factor, Γ as a function of PV and Φ, and (b) that of only PV. The vertical bars in (b) represent 95% confidence interval. The averaging is carried out for the $\Gamma < 10$ to avoid averaging outliers. This choice can alter the resultant average Γ but the average Γ with no data exclusion does not exceed 1.

Supplementary References

1. Usui, N., Wakamatsu, T., Tanaka, Y., Hirose, N., Toyoda, T., Nishikawa, S., Fujii, Y., Takatsuki, Y., Igarashi, H., Nishikawa, H., et al. (2017): Four-dimensional variational ocean reanalysis: a 30-year high-resolution dataset in the western North Pacific (FORA-WNP30). *J. Oceanogr.*, 73, 205–233.
2. Pollard, R. T. & Millard, R. C. (1970): Comparison between observed and simulated wind-generated inertial oscillations. *Deep. Sea-Res.* 17, 813–821.
3. Saito, K. *et al*. (2006): The operational JMA nonhydrostatic mesoscale model. *Mon. Weather. Rev.* **134**, 1266–1298.
4. Mooers, C. N. Several effects of baroclinic current on the cross-stream propagation of inertial-internal waves. *Geophys. Fluid. Dyn.* **6**, 245–275 (1975).
5. Kunze, E. Near-inertial wave propagation in geostrophic shear. *J. Phys. Oceanogr.* **15**, 544–565 (1985).
6. Whitt, D. & Thomas, L. Near-inertial waves in strongly baroclinic currents. *J. Phys. Oceanogr.* **43**, 706–725 (2013).
7. Thomas, L. N, Taylor, J. R., Ferrari, R. & Joyce, T. M. Symmetric instability in the Gulf Stream. *Deep-Sea Res. II* **91**, 96–110 (2013).